
Direct-Drive Cryogenic Target Implosion Performance on OMEGA

Introduction

In the direct-drive inertial confinement fusion (ICF)¹ concept, a spherical capsule containing thermonuclear fuel is imploded by the direct illumination of laser beams focused on the surface of the capsule in a near-uniform pattern. The capsule can also be mounted in a high-Z cavity, generally referred to as a hohlraum, which is then heated by the laser beams, producing a uniform radiation field of x rays. In this indirect-drive ICF concept,² the x rays, rather than the laser beams, ablate the outside of the capsule and drive the implosion. While the drive uniformity with x-ray (or indirect) drive may be currently superior to that of direct drive, it is possible to couple a significantly larger fraction of the laser energy into the hydrodynamic motion of the imploding fuel with direct drive. It is possible, therefore, with direct drive to achieve temperatures and densities that are comparable to indirect drive but with considerably less laser energy.

Within a decade or so, implosions of capsules containing cryogenic-DT-fuel layers are expected to ignite and burn at the National Ignition Facility (NIF)³ currently under construction at the Lawrence Livermore National Laboratory. Independent of the drive scheme, the basic capsule concept for ignition on the NIF is a relatively thick, cryogenic-DT-fuel layer inside a thin, spherical ablator² or foam shell.⁴ At peak compression, the high areal density (ρR) of the compressed cryogenic DT fuel can support a propagating thermonuclear burn wave due to the local bootstrap heating of the DT alpha-particle energy deposited in the fuel. Although this target concept has been under development for many years, only recently have implosions of appropriately scaled, layered, cryogenic D₂ capsules on the 60-beam, 30-kJ UV OMEGA laser system⁵ at the Laboratory for Laser Energetics begun to provide important data for the validation of both direct- and indirect-drive ignition target designs for the NIF.

The OMEGA cryogenic capsules and laser-drive pulses are energy scaled from the direct-drive NIF ignition designs^{4,6,7} to provide hydrodynamically equivalent implosions (e.g., matching implosion velocities, hot-spot convergence, and

in-flight aspect ratios). The ignition design for the NIF is driven by a 1.5-MJ, high-contrast pulse shape that puts the fuel layer on an adiabat α , of approximately 3 ($\alpha \sim 3$), where α is defined as the ratio of the electron pressure in the shell to the Fermi-degenerate pressure. To achieve hydrodynamic equivalence on OMEGA, the energy absorbed by the capsule per unit mass must be approximately the same as the NIF design. Therefore, the energy scales as the volume of the capsule or (radius³), the power scales as the surface area of the capsule or (radius²), and the duration of the drive pulse scales as the capsule radius (the distance to be traveled by the shell). On the 30-kJ OMEGA laser, this leads to a cryogenic capsule radius of approximately 920 μm containing an ice layer that is approximately 100 μm thick.⁶

An analysis⁷ of the relative performance of the NIF baseline direct-drive ignition target and the scaled OMEGA cryogenic capsule design using the 2-D hydrocode *ORCHID*⁸ has shown that the performance of the two designs can be related using the stability parameter $\bar{\sigma}$, defined as

$$\bar{\sigma}^2 = 0.06 \times \sigma_\ell^2 (\ell < 10) + \sigma_\ell^2 (\ell \geq 10), \quad (1)$$

where the σ_ℓ 's are the modal rms amplitudes of the perturbations on the inner surface of the ice layer at the end of the acceleration phase. The normalized performance curves plotted as a function of the $\bar{\sigma}$ parameter for the scaled OMEGA (green circles) and the NIF (blue squares) ignition designs are shown in Fig. 93.1 for equivalent $\alpha \sim 3$ implosions. The performance curve for a similarly scaled OMEGA $\alpha \sim 4$ design is also shown (red triangles). Although the smaller OMEGA capsule is more severely disrupted due to the perturbations associated with a given value of $\bar{\sigma}$, the $\alpha \sim 3$ and $\alpha \sim 4$ curves can be used to establish performance requirements for cryogenic implosions on OMEGA that would (computationally) ensure direct-drive ignition on the NIF under equivalent uniformity conditions.

For example, the two dashed lines associated with the NIF $\alpha \sim 3$ and OMEGA $\alpha \sim 4$ curves represent equivalent implo-

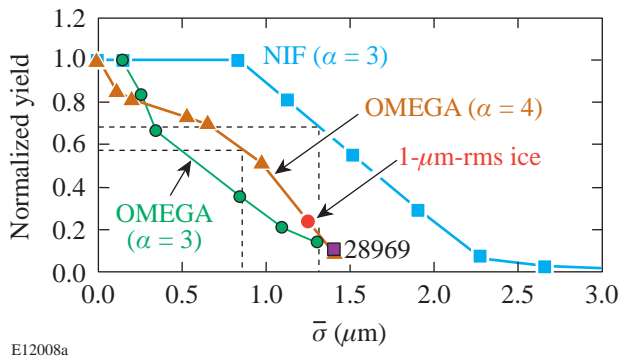


Figure 93.1

Normalized performance curves using the 2-D hydrocode *ORCHID* are shown as a function of the $\bar{\sigma}$ parameter for the scaled OMEGA (green circles) and the NIF (blue squares) ignition designs for equivalent $\alpha \sim 3$ implosions. The performance curve for a scaled OMEGA $\alpha \sim 4$ design is also shown (red triangles). The dashed lines on the $\bar{\sigma}$ axis represent implosions with equivalent uniformity on the NIF and on OMEGA. The point labeled as 28969 is the result of an $\alpha \sim 4$ cryogenic implosion and is discussed in the text. The value of $\bar{\sigma}$ for this implosion is based on a 2-D hydrocode calculation using the known laser and ice-surface nonuniformities, and the measured yield is used to determine the normalized yield. The point labeled as 1- μm -rms ice is based on the calculation for shot 28969 but assumes the NIF ignition specification for the inner-ice-layer-surface roughness.

sion conditions: the uniformity of the laser illumination and the outer and inner surfaces of the capsule are identical. Nonuniformities in the laser illumination and the outer surface of the capsule generate perturbation seeds that grow during the acceleration phase due to the Rayleigh–Taylor (RT) instability.^{9,10} These perturbations feed through to the inner ice surface, combine with the original ice perturbations, and continue to grow during the deceleration phase. This phase of the perturbation growth leads to mixing of cryogenic fuel into the hot spot and a subsequent reduction in the performance of the implosion. Therefore, under equivalent uniformity conditions, a normalized yield of 55%–60% on OMEGA ($\alpha \sim 4$) would correspond to achieving a normalized yield of approximately 70% on the NIF ($\alpha \sim 3$). Much of the work on cryogenic implosions on OMEGA is focused on achieving uniformity conditions in both the laser and the surface of the cryogenic fuel that will correspond to ignition conditions expected on the NIF.

To help achieve these conditions, a standard capsule design has been adopted to minimize variations in the fabrication process (filling, layering, and characterization). A standard low-adiabat pulse shape was also adopted for ease of data comparison among implosions with differing levels of inner ice smoothness. The pulse shape was designed to put the

cryogenic-fuel shell on an adiabat of approximately 4 (this capsule and drive pulse were used to generate the OMEGA $\alpha \sim 4$ curve shown in Fig. 93.1).

Details of the capsule design and pulse shape are discussed in the next section. The remaining three sections in this article (1) discuss experimental results from two different adiabat implosions and compare them with 1-D and 2-D hydrocode predictions; (2) discuss laser system and Cryogenic Target Handling System (CTHS) improvements that are expected to lead to ignition-equivalent implosions with cryogenic DT capsules in the near future; and (3) present conclusions.

Experimental

1. Cryogenic Target Design

The “standard” cryogenic capsule design and the low-adiabat pulse shape for the experiments reported in this article are shown in Fig. 93.2 along with the NIF direct-drive ignition point design. The shell material is either strong GDP (a high-strength plastic) or CD¹¹ and is typically $5.0 \pm 0.1 \mu\text{m}$ thick. When permeation filled with approximately 1200 atm of D₂ and then cooled to the triple point (18.73 K), the resulting ice-layer thickness is $100 \mu\text{m}$. This shell is somewhat thicker than the capsule designs scaled from the baseline 1.5-MJ ignition design for the NIF and described in Ref. 12. The thicker shell was chosen to increase the laser absorption with the low-adiabat drive pulses (the average atomic number is higher for CH than for the D₂ ice and the thicker CH shell is ablated away later in the drive pulse) and to reduce the length of time required to fill and cool the capsules with D₂ fuel (a thicker shell is more robust). A corresponding thick-plastic-shell (17- μm) ignition design for the NIF has also been developed¹³ to take advantage of the higher absorption. By tailoring the adiabat in the shell and fuel, the expected increase in imprint perturbation growth for such a thick shell is substantially reduced. Therefore, the higher absorption and hydrodynamic efficiency lead to improved ignition performance with the additional advantage of the superior mechanical properties of a much thicker shell.

While the relatively low stability of the OMEGA $\alpha \sim 3$ design in Fig. 93.1 would provide enhanced performance sensitivity to nonuniformities for parametric studies and comparison to implosion models, the current levels of laser system nonuniformity would dominate the performance of this capsule design. To enhance the performance margin of cryogenic implosions on OMEGA, a pulse shape was developed that puts the fuel layer of the standard capsule described above at $\alpha \geq 4$. An analysis of the performance of this capsule and pulse

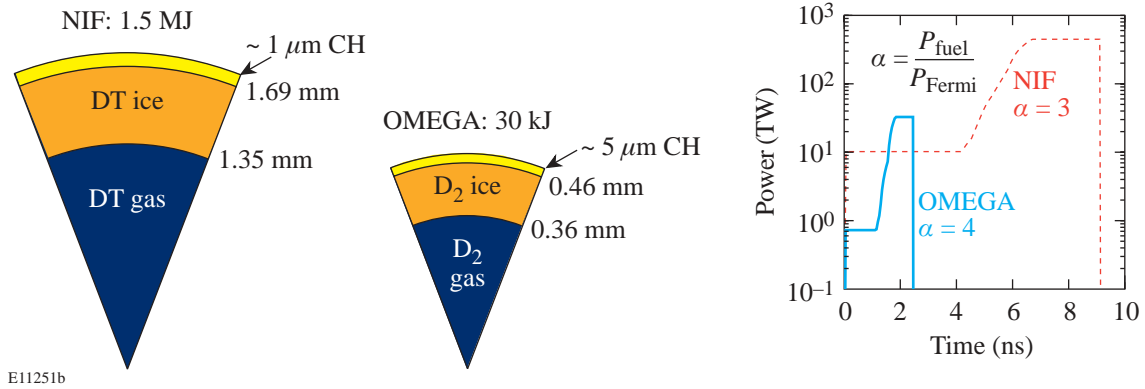


Figure 93.2

The baseline direct-drive ignition design for the NIF is shown along with the energy-scaled, hydrodynamically equivalent cryogenic design imploded on OMEGA and reported in this article. The right-hand panel shows the $\alpha \sim 3$ and $\alpha \sim 4$ pulse shapes for the NIF ignition design and the OMEGA cryogenic implosions, respectively.

shape with a stability postprocessor¹⁴ indicates that the mix width at the end of the acceleration phase is approximately 40%, considerably smaller than the 60% estimated for the scaled $\alpha \sim 3$ OMEGA design. Here the mix width is simply the peak-to-valley of the RT-growth amplitudes, and the ratio of the mix width to the shell thickness is a measure of the shell stability. For equivalent uniformity, the $\alpha \sim 4$ design should perform significantly better than the $\alpha \sim 3$ design. This is demonstrated in Fig. 93.1: the equivalent scaling to ignition performance requires a normalized yield of 55%–60% for this design compared with only 30% for the scaled $\alpha \sim 3$ design. Since an $\alpha \sim 4$ pulse shape applied to the 1.5-MJ NIF baseline direct-drive design still leads to ignition,⁴ the OMEGA $\alpha \sim 4$ design described above should be adequate to validate ignition-equivalent performance on OMEGA.

A thorough description of the layering and shadowgraphic characterization of cryogenic capsules is given in Ref. 12. Up to four thin-shell capsules are filled and cooled in the Fill/Transfer Station (FTS) and then individually loaded into moving cryostat transfer carts (MCTC's). These carts contain all of the necessary systems to create, manipulate, and maintain an ice layer inside the plastic capsule. The capsule is located inside a small layering sphere that has four viewing ports and an opening for a laser fiber to deliver up to 150 mW of 3.16- μm IR laser power to the inside surface of the layering sphere. This IR energy is preferentially absorbed in the D_2 -ice layer, and low-pressure (~ 100 -mTorr) helium exchange gas conducts heat from the capsule to the layering sphere, which is maintained at approximately 15 K. The settings for the exchange gas pressure, the layering sphere temperature, and

the IR laser power control the layering rate of the ice. Thin sapphire windows on the viewing ports provide two orthogonal views of the capsule for shadowgraphic analysis of the layer quality and later alignment at target chamber center for implosion experiments. At shot time, the cryogenic assembly containing the layering sphere (the shroud) is rapidly removed, exposing the capsule, still mounted to the MCTC, to the laser beams. The delay between the shroud removal and laser interaction is approximately 50 ms.

While early 60-beam cryogenic capsule implosions (reported in Ref. 8) were characterized by a single shadowgraphic view,¹² recent improvements to the characterization station permit the capsule to be rotated $\pm 180^\circ$ to obtain multiple views of the inner-ice-surface quality. Although multiple views do not provide a true three-dimensional picture of the inner ice surface, an average over multiple views does provide a more accurate representation of the modal structure of the ice for 2-D simulations. For most targets, a layer is characterized by at least four views. Techniques are being developed to construct a 3-D representation of the ice layer from multiple (up to 12) 2-D shadowgraphic measurements.

A well-layered capsule is produced in approximately 24 h. Much of this time is spent searching for the triple-point isotherm in the capsule by slowly varying the IR power delivered to the layering sphere while the temperature of the layering sphere and pressure of the exchange gas are held constant. Once the settings for the triple point have been identified, a sub-10- μm -rms layer can usually be formed quickly and the modal structure will slowly anneal with time

(hours). Occasionally, a near-single-crystal layer can be grown, and these capsules generally have very smooth layers (the total rms of modes greater than 3 is about $1\ \mu\text{m}$). Figure 93.3 shows an example of two near-single-crystal-layer capsules and their multiview-averaged power spectra. Both of these capsules were imploded on the OMEGA laser system.

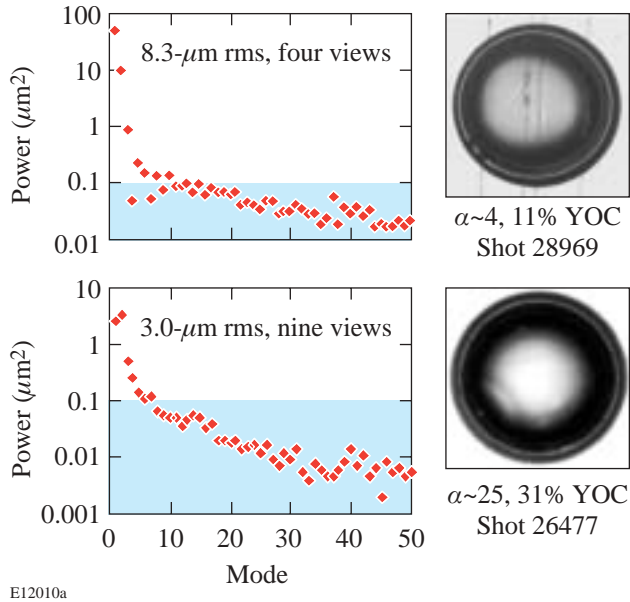


Figure 93.3
Shadowgraphs of two layered and fully characterized cryogenic D_2 capsules prior to being imploded on OMEGA. The average power spectra for the modal structure of the inner ice surface just prior to the implosions are also shown.

2. Laser-Drive Pulses

Cryogenic capsules have been imploded using two pulse shapes: a high-adiabat ($\alpha \sim 25$), 23-kJ, 1-ns square pulse (~ 0.5 -TW peak intensity) and a low-adiabat ($\alpha \sim 4$), 17-kJ, 2.5-ns shaped pulse. The $\alpha \sim 4$ pulse shape is shown in Fig. 93.2. Full single-beam smoothing was applied during all pulses by using distributed phase plates (DPP's),¹⁵ polarization smoothing (PS) with birefringent wedges,¹⁶ and 2-D, single-color-cycle, 1-THz smoothing by spectral dispersion (SSD).¹⁷ Perturbations seeded by single-beam nonuniformities experience RT growth during the acceleration phase, initiated by the arrival of the rarefaction wave (traveling outward from the inner ice surface) at the ablation surface. Since the rarefaction wave does not reach the ablation surface before the end of the high-adiabat pulse (1-ns square), the implosion performance is not particularly sensitive to the acceleration-phase perturbations introduced by laser system imprint (i.e., the acceleration phase is short). The resulting

higher performance generally leads to improved diagnostic measurements for comparison to 1-D and 2-D hydrocodes. Implosion performance with the low-adiabat, $\alpha \sim 4$ pulse is considerably more sensitive to imprint. There is less stabilization during the foot of the pulse (see Fig. 93.2) due to the lower ablation velocity. This leads to greater perturbation amplitudes at the end of the acceleration phase that feed through to the inner ice surface and continue to grow during the deceleration phase.

3. Target Alignment

The cryogenic capsules are suspended on a web of spider silks across a "C"-style mount.¹⁸ The C is designed to avoid intercepting the beams, and the use of spider silk minimizes both mass perturbations on the capsule surface that might affect implosion performance and thermal perturbations that might affect the D_2 -ice-layering process. Cryogenic capsule alignment inside the OMEGA target chamber utilizes the Target Viewing System (TVS). Each of the two orthogonal TVS lines of sight views the capsule through six independently mounted sapphire windows. These windows provide the only optical access to the layering sphere through the various thermal barriers. The alignment accuracy of the TVS to target chamber center (TCC) is better than $5\ \mu\text{m}$ for noncryogenic, stalk-mounted targets. The alignment accuracy for cryogenic capsules, however, is limited due to focal blurring through the sapphire windows; for cryogenic capsules, the alignment accuracy is estimated to be approximately $10\ \mu\text{m}$.

In addition to blurring the capsule images in the TVS, it was found that the target optical offset (the difference between the capsule location viewed through the sapphire windows and the actual location of the capsule) established at room temperature, $< 5\ \mu\text{m}$, during the assembly of the MCTC was significantly different once the cryogenic systems were cooled. An analysis of chamber-mounted x-ray pinhole camera (XPHC) images taken during the implosions showed that virtually every cryogenic implosion prior to the identification of a target alignment problem had been offset from TCC by 60 to $120\ \mu\text{m}$. Using up to five fixed XPHC images on each shot, the magnitude and direction of the capsule offsets were determined with high accuracy. The influence of this offset on the cryogenic implosion performance is presented in the **Discussion** section.

To accurately align cryogenic capsules to TCC, a calibration procedure was developed to generate offset alignment reticles for the TVS. A stalk-mounted surrogate capsule is loaded into the MCTC, the system is cooled to the nominal operating temperature, and the surrogate capsule is inserted

into the target chamber. The capsule is aligned to the TCC using the TVS and then the shroud is removed, exposing the capsule. TVS images of the “bare” capsule are then acquired, and the optical offset caused by the sapphire windows in the shroud is calculated. This offset is then used to generate a unique alignment reticle for each MCTC.

4. Experimental Setup and Diagnostics

The primary diagnostics for cryogenic implosions include the fixed XPHC's mentioned above,¹⁹ x-ray framing cameras,²⁰ high-resolution Kirkpatrick–Baez (KB) microscopes,²¹ primary and secondary neutron yield,²² secondary proton yield,²³ the ion temperature,²⁴ and the neutron reaction history.²⁵ The energy loss of the secondary protons is used to infer the total areal density.²⁶ The XPHC's provide a low-resolution, time-integrated x-ray image of the capsule shell and core. The framing cameras provide sequential, time-gated core images from just before fusion burn until well after stagnation. These images can be used to assess time-dependent, low-mode asymmetries during the assembly of the core. The high-resolution ($\sim 5\text{-}\mu\text{m}$), time-integrated KB microscopes offer the best images of the core at peak x-ray emission. Asymmetries in the core are related to both laser system nonuniformities and low-mode inner-ice-surface structure. The primary and secondary fusion yields are the most direct measure of the capsule performance and are most sensitive to mix and ion temperature. The reaction history provides crucial validation for hydrocode performance and laser absorption, while the total areal density is perhaps the most important measure of the hydrodynamic performance of the implosion: an areal density of at least 300 mg/cm^2 is required to absorb the full energy of the DT alpha in an ignition target.

Results

As described above, most of the recent cryogenic targets have been significantly offset from TCC at the beginning of the laser pulse. Distributed phase plates (DPP's) on each of the 60 OMEGA beams are used to define the focal-spot distribution of the beams on the target. The minimum spot size of each individual beam is nominally $920\text{ }\mu\text{m}$, and the intensity distribution is a super-Gaussian of the order of 2.2. Although the effective f number of each beam with the DPP is large, the near-Gaussian intensity distribution imposes a large intensity perturbation on the surface of the capsule when the capsule is offset from the nominal best focus of all 60 beams (each of the beams is independently pointed to an alignment surrogate at TCC with an rms deviation of less than $20\text{ }\mu\text{m}$). This laser-intensity perturbation causes the fuel shell to converge asymmetrically, significantly degrading the performance of the

implosion. For example, the peak-to-valley intensity variation on the surface of a $920\text{-}\mu\text{m}$ -diam capsule offset by $50\text{ }\mu\text{m}$ from TCC is approximately $\pm 40\%$ and climbs to nearly $\pm 70\%$ for a $100\text{-}\mu\text{m}$ offset with the standard OMEGA power balance. The effect of this offset on implosion performance is similar to a large $\ell = 1$ mode in the ice (i.e., the ice is thicker on one side of the capsule than on the other; see the capsule shadowgraph of shot 28969 in Fig. 93.3). Not only is the capsule imploded asymmetrically, but the capsule center shifts during the implosion under the influence of the greater pressure generated by the higher laser intensity on the side of the capsule closest to TCC. A higher-order, super-Gaussian, single-beam intensity profile would reduce the effect of an alignment offset and is being pursued in parallel with improvements in the target alignment procedures. Similarly, a larger focal-spot size relative to the target diameter would somewhat mitigate the alignment sensitivity but at the expense of energy loss around the target.

After developing the target alignment procedure described above, several implosions were performed with the capsule less than $25\text{ }\mu\text{m}$ from TCC at the start of the laser pulse. The performance of these implosions can be simulated using the 2-D hydrocode *DRACO*.²⁷ A comparison will be made between the performance of two cryogenic target implosions (shots 28900 and 28969) and *DRACO* simulations. Shot 28900 imploded a $100\text{-}\mu\text{m}$ -thick D_2 -ice layer with a $6.5\text{-}\mu\text{m}$ -rms inner ice layer (pre-shot characterization) using a high-adiabat ($\alpha \sim 25$), 1-ns square pulse with a UV energy on target of 23.3 kJ and an rms energy variation among the 60 OMEGA beams of 2.9%. Shot 28969 imploded a $100\text{-}\mu\text{m}$ -thick D_2 -ice layer with an $8.3\text{-}\mu\text{m}$ -rms inner ice layer dominated by the $\ell = 1$ component (see Fig. 93.3 and the modal spectrum for this capsule); the measured rms energy variation of the beams was 3.4% and the low-adiabat $\alpha \sim 4$ pulse shape delivered 16.6 kJ to the target. Analysis of the PHC data showed that both capsules were offset from TCC by less than $20\text{ }\mu\text{m}$ at the beginning of the laser pulse. Although the effect of this small offset on the implosion performance is not negligible (especially for the low-adiabat drive pulse), it does not dominate the performance. The 2-D *DRACO* simulations neglect the offset, and the predicted performance is based entirely on the laser system power balance and the quality of the inner surface of the ice layer.

Figures 93.4 and 93.5 show the 2-D *DRACO* predictions for the fuel-density contours [panel (a)] and a polar lineout of the total areal density [panel (b)] for the two implosions. It is immediately apparent that both cores have been offset by the

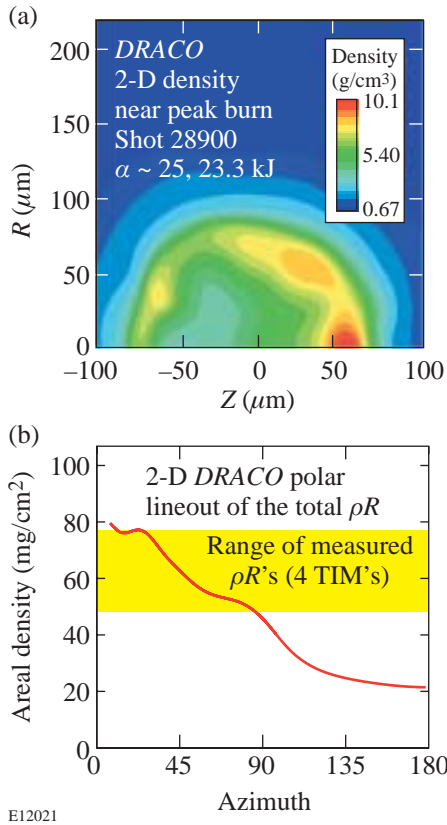


Figure 93.4 (a) A plot of the fuel-density contours at peak burn for shot 28900 ($\alpha \sim 25, 23.3$ kJ) from the 2-D hydrocode *DRACO*. (b) Polar lineout of the total areal density from the center of the core derived from the density contours shown in (a). The yellow region shows the range of the individual areal-density measurements inferred from the average energy loss of secondary protons.

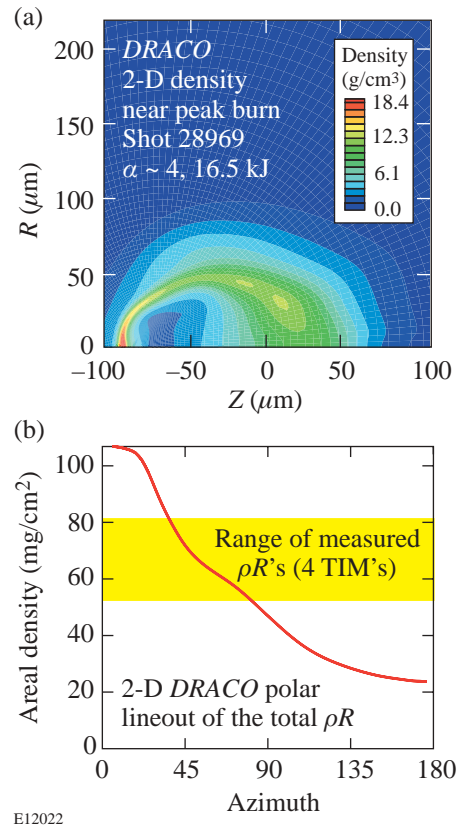


Figure 93.5 (a) A plot of the fuel-density contours at peak burn for shot 28969 ($\alpha \sim 4, 16.5$ kJ) from the 2-D hydrocode *DRACO*. (b) Polar lineout of the total areal density from the center of the core derived from the density contours shown in (a). The yellow region shows the range of the individual areal-density measurements inferred from the average energy loss of the secondary protons.

influence of the low-mode nonuniformity of the ice layers. The effect of the large $\ell = 1$ mode on the inner ice surface in shot 28969 is especially apparent in Fig. 93.5(a). The core offsets lead to a significant asymmetry in the predicted areal density. The areal densities predicted by the 2-D simulations agree well with the measured values, which fall within the yellow regions in Figs. 93.4(b) and 93.5(b). It is not currently possible to correlate the polar angles of the areal-density lineouts from either shot with the orientation of the experimental measurements. However, the roughly factor-of-5 variation in the 2-D areal density for shot 28969 (and the factor-of-4 variation for shot 28900) is consistent with some of the experimental variations measured on other implosions in which the capsule was significantly offset from TCC. The extreme values of areal density are not likely to be observed on most shots with only a limited number of individual measurements (typically four per shot) available.

Table 93.I gives a comparison between experimentally measured or inferred quantities and the 1-D *LILAC*²⁸ and 2-D *DRACO* predictions. The 1-D yield from shot 28900 ($\alpha \sim 25$) is considerably higher than the 2-D *DRACO* yield (57% of the 1-D value) and virtually identical to the measured yield. This suggests that the at-shot state of the capsule may have been different from the pre-shot characterization used in the 1-D and 2-D hydrocodes. Assuming that the temperature of the capsule might have changed prior to the shot (evidence for this is discussed in the following section), a series of 1-D *LILAC* calculations were performed in which the temperature of the capsule was varied above and below the nominal value from the pre-shot characterization (typically 100 mK below the triple point). These simulations did not provide a satisfactory explanation for the high performance of the capsule relative to the 2-D predictions (the yield was nearly a factor of 4 higher than any previous $\alpha \sim 25$ implosion with $\sim 100 \mu m$ of ice; the

Table 93.I: A comparison of the experimental measurements with the 1-D and 2-D hydrocode predictions. The hydrocode predictions are given as the ratio of the experimental measurement to the predicted value (in percent).

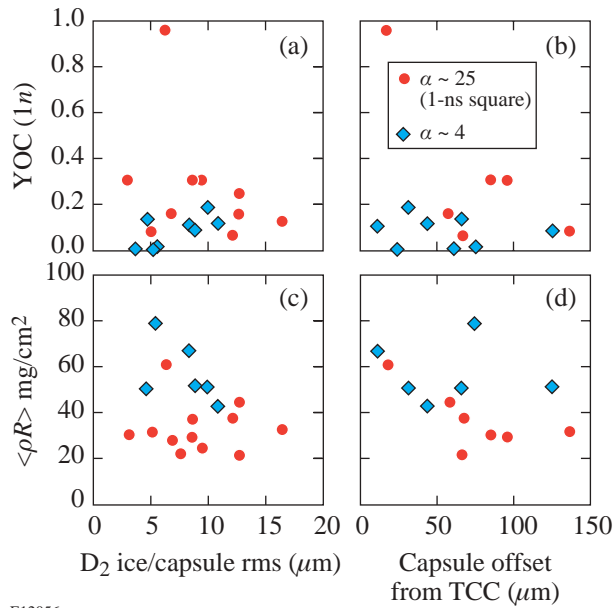
| Measurement | Shot 28900 | Experimental/ 1-D <i>LILAC</i> (%) | Experimental/ 2-D <i>DRACO</i> (%) | Shot 28969 | Experimental/ 1-D <i>LILAC</i> (%) | Experimental/ 2-D <i>DRACO</i> (%) |
|---|-----------------------|---------------------------------------|---------------------------------------|--------------------|---------------------------------------|---------------------------------------|
| Primary neutron yield | 1.27×10^{11} | 96 | 171 | 5.95×10^9 | 11 | 112 |
| Secondary neutron yield | 1.17×10^9 | 84 | 132 | 6.75×10^7 | 9.7 | 107 |
| Secondary proton yield | 2.03×10^8 | 112 | | 7.14×10^6 | 11 | |
| $\langle \rho R \rangle$ mg/cm ² | 61 | 133 | 120 | 67.00 | 84 | 115 |
| T_{ion} (keV) | 3.6 | 157 | 139 | 2.5 | 145 | 125 |
| Y_{2n}/Y_{1n} | 0.0092 | 85 | 77 | 0.0113 | 91 | 95 |
| Y_{2p}/Y_{1p} | 0.0016 | 114 | | 0.0012 | 104 | |
| Offset (μm) | 14 | | | 11 | | |

primary difference from previous shots is the small TCC offset). A further series of calculations were performed in which the flux limiter²⁹ was increased from 0.060 to 0.068. This increased the 1-D yield by a factor of 2, lowering the yield-over-clean (YOC) to approximately 50% and bringing the predicted neutron bang time into agreement with the measured value. A similar treatment within *DRACO* would have a comparable result and bring the 2-D yield prediction into agreement with the experimental measurement. While a higher value of the flux limiter for this shot is suggested by the bang-time measurement, a change in the flux limiter is not supported by recent absorption measurements on CH at OMEGA. In contrast to shot 28900, the 2-D yield for shot 28969 ($\alpha \sim 4$) is in very good agreement with the experimental measurement. Both are approximately 10% of the 1-D yield. Indeed, all of the 2-D predictions are reasonably close to the experimental measurements for this shot. This is a very encouraging result given the large amplitude of the low-mode nonuniformity on the inner ice surface layer.

Figure 93.6 shows the primary neutron YOC and the average total areal density as a function of the measured capsule offset and the pre-shot characterization of the D₂ inner-ice-surface rms for all of the cryogenic implosions to date in which the ice layer appears to have been intact at shot time. Based on the analysis shown in Fig. 93.1, the primary yield is expected to increase with increasing smoothness of the inner ice layer [Fig. 93.6(a)]. For most of the shots, the influence of the ice-surface perturbations on the implosion performance

is obscured by the gross low-mode nonuniformity caused by the capsule offset [Fig. 93.6(b)]. With no capsule characterization in the target chamber prior to the shot, there is also uncertainty in the inner-ice-surface roughness at shot time. In Fig. 93.6(b), there is evidence with the high-adiabat implosions that the capsule performance is significantly degraded due to the capsule offset. As expected, the average total areal density for the high-adiabat implosions does not appear to depend on the ice-layer quality [Fig. 93.6(c)]; however, there appears to be a correlation for increasing total areal density with decreasing ice roughness for the low-adiabat ($\alpha \sim 4$) implosions, where the convergence ratio at stagnation is expected to be somewhat larger. As a function of decreasing capsule offset from TCC, there is a general trend of increasing areal density for both the low- and high-adiabat implosions [Fig. 93.6(d)]. This also correlates with the observation that the asymmetry in the individual areal-density measurements (the spread divided by the mean) decreases with decreasing target offset.

The measured ion temperatures in all of the cryogenic implosions exceed the 1-D hydrocode predictions. In the absence of a significant shock yield (there is no evidence for a shock yield from the neutron temporal diagnostic), this is usually understood as a phenomenon associated with the mixing of cold fuel into the hot spot. The measured yield preferentially samples the small hot-spot volume, which is surrounded by a steep, mix-induced temperature gradient. The yield from this mix region is considerably less than the ratio of the fuel



E12056

Figure 93.6

(a) The ratio of the primary neutron yield to the predicted yield from the 1-D hydrocode *LILAC* [the yield-over-clean (YOC)] as a function of the pre-shot D_2 -ice roughness. (b) The same YOC values plotted as a function of the capsule offset from TCC [for some of the points shown in panel (a), the offset was not measured] at the start of the laser pulse. (c) The average areal density as a function of the pre-shot D_2 -ice roughness. Increasing areal density appears to be correlated with a reduction in the inner-ice-surface roughness for the low-adiabat implosions. Such a correlation does not exist for the high-adiabat implosions that are expected to be much less sensitive to laser imprint and acceleration-phase perturbation growth. (d) The average areal density as a function of the capsule offset from TCC. For both low- and high-adiabat implosions, the areal density increases with decreasing capsule offset.

volumes (hot spot and mix regions). However, the large offsets and uncertainties in the layer quality at shot time make it difficult to interpret the ion temperature data. For example, the average ion temperature measured for implosions where other experimental evidence (e.g., reaction histories and core images) suggests that the ice layer was compromised prior to the shot is 4.4 keV and only 2.7 keV for implosions in which the experimental evidence suggests an intact layer. In Table 93.I, the measured ion temperatures for the two implosions suggest some degree of mix when compared with the hydrocode predictions.

Finally, secondary proton production in shots 28900 and 28969 indicate a hot-spot areal density between 10 and 12 mg/cm² according to the uniform density model of Azechi and Cable.³⁰ The hot-spot areal density inferred from shot 28900 ($\alpha \sim 25$) is somewhat larger than that inferred for the lower-

adiabat implosion. These hot-spot areal densities are about a factor of 2 larger than those reported in Ref. 12 and are at or near the saturation limit of the model for the measured ion temperatures.

Discussion

The rms amplitudes of the inner-ice-surface roughness at the end of the acceleration phase in the 2-D *DRACO* simulation of shot 28969 ($\alpha \sim 4$) can be used to calculate the value of the $\bar{\sigma}$ parameter used by McKenty⁷ to define the scaling performance of cryogenic implosions on OMEGA and the NIF. This point falls very close to the OMEGA $\alpha \sim 4$ curve in Fig. 93.1 and should be compared with the point labeled as 1- μm -rms ice. The 1- μm -rms ice point represents an identical 2-D simulation (i.e., current laser system nonuniformity on OMEGA) assuming the NIF specification for ice smoothness (total rms of 1 μm). This comparison clearly shows that scaled ignition performance on OMEGA will require improvements in the OMEGA laser system uniformity as well as improvements to the inner-ice-layer smoothness. Achieving ignition-equivalent performance on OMEGA (e.g., a normalized 2-D yield of approximately 60%) will require a laser system nonuniformity of 1% or less and an rms inner-ice-surface roughness of approximately 1 μm .

Although outstanding inner-ice-layer smoothness has been achieved (approximately 3- μm rms including contributions from the thin plastic shell; see also Fig. 93.2), the stability of the IR laser used to layer the D_2 ice and the fiber-optic transport used to deliver IR power to the layering sphere does not appear to be adequate to produce and maintain high-surface-quality layers (sub-3- μm rms). An IR power feedback control system based on the measured power into the layering sphere is currently being implemented to establish the triple point to the required accuracy (a high-quality layer requires single-crystal growth within approximately 1 mK of the triple point). The goal of the feedback system is to regulate the power in the layering sphere to 0.1%.

As described in the previous section, improvements to the laser system uniformity include the development of new distributed phase plates (DPP's) with tight tolerances on spot size, ellipticity, and order; new techniques for enhanced power balance³¹ and target alignment; and new specifications for beam pointing. Based on measurements of the prototype DPP, an analysis of the potential improvements to the overall laser system nonuniformity suggests that the requirement for <1% rms will be achieved in the near future. Low-adiabat drive pulses that include a picket to tailor the adiabat across the

cryogenic fuel shell are expected to significantly reduce the imprint and subsequent growth rates from single-beam nonuniformities.¹³ By tailoring the adiabat with a picket pulse, the ablation velocity can be increased without significantly raising the internal pressure of the capsule. This helps to minimize the growth of imprint perturbations during the acceleration phase. A future study of cryogenic capsule performance with and without these pickets is one of the highest priorities within the direct-drive program at LLE.

Conclusions

The performance of hydrodynamically scaled cryogenic ignition capsules with both low- and high-adiabat pulse shapes has been reported. The primary goal of these experiments is to demonstrate equivalent direct-drive ignition performance using pulse shapes and capsule designs scaled from the baseline ignition design for the NIF. Near 1-D hydrocode performance has been measured with a high-adiabat ($\alpha \sim 25$) drive pulse on a capsule containing a 100- μm -thick layer of cryogenic D_2 , and near 2-D hydrocode performance has been measured on a similar capsule with a low-adiabat ($\alpha \sim 4$) drive. The fabrication and the characterization of layered cryogenic capsules with inner-ice-surface roughness of between 3- and 12- μm rms are now routine (see Fig. 93.3). A new cryogenic target characterization diagnostic is under development to provide a single view of the inner ice surface within 50 ms of the shot. A feedback system is being developed to stabilize the IR laser power in the layering sphere. These upgrades will significantly improve implosion performance in future cryogenic experiments. Additionally, improvements to the overall laser system uniformity are being pursued. These include the development of a new distributed phase plate with a high-order super-Gaussian intensity profile and much tighter tolerances on plate-to-plate spot size and ellipticity. These new DPP's will immediately reduce the overall laser system power imbalance. Coupled with more-accurate UV energy transport measurements and tighter tolerances on beam pointing, the overall laser system nonuniformity should approach 1% rms. With this level of laser system uniformity and continued improvements in the inner-ice-surface smoothness, it will be possible to validate the performance of direct-drive ignition capsule designs on OMEGA.

ACKNOWLEDGMENT

The authors are grateful to the staff of the Laboratory for Laser Energetics for their tireless dedication to the cryogenic implosion program and the operation of the OMEGA laser system. In particular, the authors would like to acknowledge the efforts of the Cryogenic Target Fabrication Group for the production of layered and characterized capsules on a regular schedule. This work was supported by the U. S. Department of Energy Office of Inertial

Confinement Fusion under Cooperative Agreement No. DE-FC03-92SF19460, the University of Rochester, and the New York State Energy Research and Development Authority. The support of DOE does not constitute an endorsement by DOE of the views expressed in this article.

REFERENCES

1. J. Nuckolls *et al.*, *Nature* **239**, 139 (1972).
2. J. D. Lindl, *Inertial Confinement Fusion: The Quest for Ignition and Energy Gain Using Indirect Drive* (Springer-Verlag, New York, 1998).
3. W. J. Hogan, E. I. Moses, B. E. Warner, M. S. Sorem, and J. M. Soures, *Nucl. Fusion* **41**, 567 (2001).
4. S. E. Bodner, D. G. Colombant, J. H. Gardner, R. H. Lehmborg, S. P. Obenschain, L. Phillips, A. J. Schmitt, J. D. Sethian, R. L. McCrory, W. Seka, C. P. Verdon, J. P. Knauer, B. B. Afeyan, and H. T. Powell, *Phys. Plasmas* **5**, 1901 (1998).
5. T. R. Boehly, D. L. Brown, R. S. Craxton, R. L. Keck, J. P. Knauer, J. H. Kelly, T. J. Kessler, S. A. Kumpan, S. J. Loucks, S. A. Letzring, F. J. Marshall, R. L. McCrory, S. F. B. Morse, W. Seka, J. M. Soures, and C. P. Verdon, *Opt. Commun.* **133**, 495 (1997).
6. Laboratory for Laser Energetics LLE Review **79**, 121, NTIS document No. DOE/SF/19460-317 (1999). Copies may be obtained from the National Technical Information Service, Springfield, VA 22161.
7. P. W. McKenty, V. N. Goncharov, R. P. J. Town, S. Skupsky, R. Betti, and R. L. McCrory, *Phys. Plasmas* **8**, 2315 (2001).
8. R. L. McCrory and C. P. Verdon, in *Inertial Confinement Fusion*, edited by A. Caruso and E. Sindoni (Editrice Compositori, Bologna, Italy, 1989), pp. 83–124.
9. Lord Rayleigh, *Proc. London Math Soc.* **XIV**, 170 (1883).
10. G. Taylor, *Proc. R. Soc. London Ser. A* **201**, 192 (1950).
11. A. Nikroo *et al.*, *Fusion Sci. Technol.* **41**, 214 (2002).
12. C. Stoeckl, C. Chiritescu, J. A. Delettrez, R. Epstein, V. Yu. Glebov, D. R. Harding, R. L. Keck, S. J. Loucks, L. D. Lund, R. L. McCrory, P. W. McKenty, F. J. Marshall, D. D. Meyerhofer, S. F. B. Morse, S. P. Regan, P. B. Radha, S. Roberts, T. C. Sangster, W. Seka, S. Skupsky, V. A. Smalyuk, C. Sorce, J. M. Soures, R. P. J. Town, J. A. Frenje, C. K. Li, R. D. Petrasso, F. H. Séguin, K. Fletcher, S. Padalino, C. Freeman, N. Izumi, R. Lerche, and T. W. Phillips, *Phys. Plasmas* **9**, 2195 (2002).
13. V. N. Goncharov, "Improved Performance of Direct-Drive ICF Target Designs with Adiabat Shaping Using an Intensity Picket," to be published in *Physics of Plasmas*; see also this issue of the LLE Review, p. 18.
14. V. N. Goncharov, P. McKenty, S. Skupsky, R. Betti, R. L. McCrory, and C. Cherfils-Clérouin, *Phys. Plasmas* **7**, 5118 (2000).
15. T. J. Kessler, Y. Lin, J. J. Armstrong, and B. Velazquez, in *Laser Coherence Control: Technology and Applications*, edited by H. T. Powell and T. J. Kessler (SPIE, Bellingham, WA, 1993), Vol. 1870, pp. 95–104.

16. T. R. Boehly, V. A. Smalyuk, D. D. Meyerhofer, J. P. Knauer, D. K. Bradley, R. S. Craxton, M. J. Guardalben, S. Skupsky, and T. J. Kessler, *J. Appl. Phys.* **85**, 3444 (1999).
17. S. Skupsky, R. W. Short, T. Kessler, R. S. Craxton, S. Letzring, and J. M. Soures, *J. Appl. Phys.* **66**, 3456 (1989).
18. Laboratory for Laser Energetics LLE Review **81**, 21, NTIS document No. DOE/SF/19460-335 (1999). Copies may be obtained from the National Technical Information Service, Springfield, VA 22161.
19. F. J. Marshall, T. Ohki, D. McInnis, Z. Ninkov, and J. Carbone, *Rev. Sci. Instrum.* **72**, 713 (2001).
20. D. K. Bradley *et al.*, *Rev. Sci. Instrum.* **66**, 716 (1995).
21. F. J. Marshall and J. A. Oertel, *Rev. Sci. Instrum.* **68**, 735 (1997); F. J. Marshall, M. M. Allen, J. P. Knauer, J. A. Oertel, and T. Archuleta, *Phys. Plasmas* **5**, 1118 (1998).
22. V. Yu. Glebov, D. D. Meyerhofer, C. Stoeckl, and J. D. Zuegel, *Rev. Sci. Instrum.* **72**, 824 (2001); M. D. Cable and M. B. Nelson, *Rev. Sci. Instrum.* **59**, 1738 (1988).
23. F. H. Séguin, C. K. Li, D. G. Hicks, J. A. Frenje, K. M. Green, R. D. Petrasso, J. M. Soures, D. D. Meyerhofer, V. Yu. Glebov, C. Stoeckl, P. B. Radha, S. Roberts, C. Sorce, T. C. Sangster, M. D. Cable, S. Padalino, and K. Fletcher, *Phys. Plasmas* **9**, 2725 (2002).
24. T. J. Murphy, R. E. Chrien, and K. A. Klare, *Rev. Sci. Instrum.* **68**, 610 (1997); R. A. Lerche *et al.*, *Appl. Phys. Lett.* **31**, 645 (1977).
25. C. Stoeckl, V. Yu. Glebov, S. Roberts, T. C. Sangster, R. A. Lerche, R. L. Griffith, and C. Sorce, to be published in the Review of Scientific Instruments; see also Laboratory for Laser Energetics LLE Review **92**, 156, NTIS document No. DOE/SF/19460-465 (2002). Copies may be obtained from the National Technical Information Service, Springfield, VA 22161.
26. F. H. Séguin, C. K. Li, J. A. Frenje, S. Kurebayashi, R. D. Petrasso, F. J. Marshall, D. D. Meyerhofer, J. M. Soures, T. C. Sangster, C. Stoeckl, J. A. Delettrez, P. B. Radha, V. A. Smalyuk, and S. Roberts, *Phys. Plasmas* **9**, 3558 (2002).
27. P. B. Radha, V. N. Goncharov, T. J. B. Collins, J. A. Delettrez, and P. W. McKenty, "Multidimensional Effects in Plastic Shell Implosions on the OMEGA Laser," to be submitted to *Physics of Plasmas*.
28. M. C. Richardson, P. W. McKenty, F. J. Marshall, C. P. Verdon, J. M. Soures, R. L. McCrory, O. Barnouin, R. S. Craxton, J. Delettrez, R. L. Hutchison, P. A. Jaanimagi, R. Keck, T. Kessler, H. Kim, S. A. Letzring, D. M. Roback, W. Seka, S. Skupsky, B. Yaakobi, S. M. Lane, and S. Prussin, in *Laser Interaction and Related Plasma Phenomena*, edited by H. Hora and G. H. Miley (Plenum Publishing, New York, 1986), Vol. 7, pp. 421–448.
29. R. C. Malone, R. L. McCrory, and R. L. Morse, *Phys. Rev. Lett.* **34**, 721 (1975).
30. H. Azechi, M. D. Cable, and R. O. Stapf, *Laser Part. Beams* **9**, 119 (1991); M. D. Cable and S. P. Hatchett, *J. Appl. Phys.* **62**, 2233 (1987).
31. Laboratory for Laser Energetics LLE Review **91**, 116, NTIS document No. DOE/SF/19460-458 (2002). Copies may be obtained from the National Technical Information Service, Springfield, VA 22161.